INTEGRATED MANOEUVRE DETECTION AND ESTIMATION USING NONLINEAR KALMAN FILTERS DURING ORBIT DETERMINATION OF SATELLITES

C. Bergmann[(1)], A. Zollo[(1)], J. Herzog[(1)], and T. Schildknecht[(2)]

[(1)]*Deutsches Zentrum für Luft- und Raumfahrt, Münchener Str. 20, 82234 Weßling, Germany, Email: christoph.bergmann@dlr.de*

[(2)]*Astronomisches Institut, Universität Bern, Sidlerstr. 5, 3012 Bern, Switzerland*

ABSTRACT

We present our approach to automatically detect and characterize satellite manoeuvres during the orbit determination (OD) process, based on passive-optical measurements of several geostationary (GEO) satellites from the SMARTnet telescope network [4].
Our technique employs a nonlinear Kalman filter (either an Extended Kalman Filter (EKF) or an Unscented Kalman Filter (UKF)) to detect unexpected deviations from the predicted states of a satellite during the OD process, and subsequently estimates the manoeuvre epoch and respective Δv-components. An immediate benefit of using nonlinear Kalman filters is that the analysis is performed directly on the angle measurements (right ascension and declination) of an object, which are derived from passive-optical observations with a telescope, as an integral part of the object identification and orbit determination / improvement processes. This mitigates the need to first calculate a new orbit, as is the case for more traditional post-orbit-determination techniques that work with time-series of orbital elements. Once a manoeuvre is detected, its epoch is estimated by means of conjunction analysis. This way we can incorporate the covariance information of the object's state estimates. More specifically, we propagate two state vectors bracketing the manoeuvre forward and backward in time, respectively. The interval between the two epochs is sampled and the encounter probability is calculated for each step. We then identify the manoeuvre epoch as the time at which the encounter probability takes on its maximum value. Once the manoeuvre epoch is known, the Δv-components of the manoeuvre can be determined by direct comparison of the two propagated states at that epoch, which also yields information about the type of manoeuvre that has occurred.
For the analysis in this study we use passive-optical measurements of two GEO satellites (ASTRA-1KR and ASTRA-1L), for which we had access to operator data including manoeuvre information. Observations were taken with the SMARTnet telescope network station near Sutherland, South Africa. We present our results of using a UKF and an EKF. For each filter, several manoeuvre indicators are employed, namely the squared and normalized residuals, the Log-Likelihood, and the Mahalanobis distance.
We demonstrate the ability to determine manoeuvre epochs accurate to within less than a minute and Δv-components to the cm/s-level.
Eventually, this automated manoeuvre detection and estimation will be applied to all measurements taken with the SMARTnet telescope network.

Keywords: manoeuvre detection; Kalman filters.

1. INTRODUCTION

In order to maintain their operational orbits, all satellites have to perform station-keeping manoeuvres on a regular basis. If left unaccounted for, satellite manoeuvres can lead to object misidentification or duplicate entries in a database of orbiting objects when the correlation of new measurements to an existing object fails. Ultimately, this can even lead to the loss of an object from the data base, if it cannot be found anymore due to inaccurate orbit estimates. Automated manoeuvre detection mitigates these problems and informs the object identification and orbit determination (OD) processes, significantly improving the accuracy in the knowledge of the orbits of the objects in the database, and minimizing the risk of confusion between nearby objects. From a Space Situational Awareness (SSA) point of view, accurate knowledge of the orbits of as many objects as possible is required to make informed decisions on possible collision avoidance manoeuvres.
For geostationary (GEO) satellites, these manoeuvres mainly consist of North-South (NS) station-keeping manoeuvres, which are out-of-plane manoeuvres that aim to keep the inclination small, and East-West (EW) station-keeping manoeuvres, which are in-plane manoeuvres that are necessary to keep the satellites at their assigned longitudinal slots. Without these manoeuvres, perturbing accelerations, mainly due to the non-spherical shape of the Earth, the gravitational pulls of the Sun and the Moon, and the effects of Solar radiation pressure, will slowly induce a longitudinal drift and an increase in

the inclination (e.g. [16], and references therein).
In order to detect these manoeuvres, a wide variety of approaches has been tried and investigated (see [15] for a comprehensive overview). For example, more traditional post-orbit determination techniques often focus on sudden changes or inconsistencies in one or more orbital elements (e.g. [11], [17]), or the difference between the predicted states before and after the addition of a new measurement (e.g. [12]). There has also been a recent study that applies a linear Kalman Filter [9] on the orbital elements, where manoeuvres can be detected by analysing the residuals [20]. Another method performs a conjunction analysis and detects manoeuvres as maxima in the estimated encounter probability [6].
Several studies have also employed an Extended Kalman Filter (EKF) and variations thereof for manoeuvre detection (e.g. [7]). More recently, the Unscented Kalman Filter (UKF) [8] has also become increasingly used as a viable alternative to the EKF for many applications (e.g. [18]).
Of course, the topic of manoeuvre detection is closely related to the problem of object association when maintaining a database of orbiting objects, as, for example, discussed by [15].
Our study aims to utilize the sequential nature of these nonlinear Kalman filters, so that manoeuvres can readily be detected during the OD phase whenever a new observation is made. This work builds upon a previous study by [20], who focused on the EKF.
We describe our data acquisition and analysis approach in Sections 2 and 3, respectively. In Section 4 we present the results of our analysis using both the UKF and the EKF for the ASTRA-1KR and ASTRA-1L satellites. We then discuss our findings in Section 5, followed by a brief outlook in Section 6.

2. OBSERVATIONS

In March and April 2019 we ran a high-cadence observational campaign for a number of geostationary satellites, for which the operator SES S.A. had kindly provided us with information about performed station keeping manoeuvres. Observations were carried out using our SMARTnet [4] telescope station near Sutherland, South Africa (see Fig. 1), resulting in several tens of thousands of measurements. Every passive-optical observation yields a pair of astrometric angle measurements (α, δ), that is, a value for right ascension and declination. Astrometric data reduction is automatically performed with the `ZimControl` software package [5].
For the analysis in this work we focus on a subset of 4755 measurements of ASTRA-1KR and 4723 measurements of ASTRA-1L, each spanning about 9.5 days from 15-25 March 2019 (UTC).

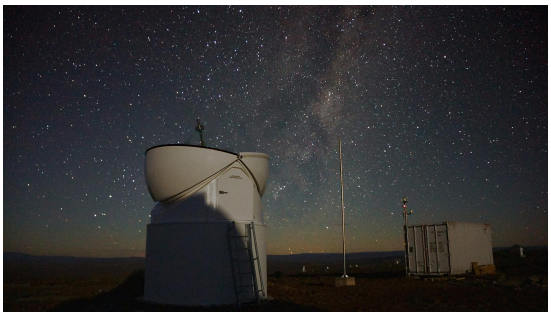

Figure 1. SMARTnet telescope station SMART-01-SUTH near Sutherland, South Africa (credits: H. Fiedler).

3. METHODOLOGY

3.1. Manoeuvre detection

We have implemented prototypes of a UKF and an EKF. These sequential filters combine our astrometric measurements with a numerically propagated model of the orbit to produce an updated orbit estimate every time a new observation is made. Because the filters do not have any a priori knowledge about manoeuvres, by comparing the expected states with the observed states, manoeuvres can be detected.
Assuming there is no control input, a valid assumption if no manoeuvres occur, we can define the *state transition function* f by

$$\bar{\mathbf{x}}_k = f(\mathbf{x}_{k-1}) \quad , \tag{1}$$

where $\bar{\mathbf{x}}_k$ denotes the *prior* state estimate at time step k, and $\mathbf{x}_{k-1}$ is the *posterior* state estimate at time step $k+1$. The implementation of f includes non-Keplerian accelerations due to a full geopotential model up to order and degree (10, 10), the gravitational pulls of the Sun and the Moon, and the Solar radiation pressure.
Similarly, we can define the *measurement function* h, which calculates right ascension and declination from the state vector and the site vector at a given epoch, by

$$\mathbf{y}_k = \mathbf{z}_k - h(\bar{\mathbf{x}}_k) \quad , \tag{2}$$

where $\mathbf{y}_k$ are the filter residuals and $\mathbf{z}_k$ are the measurements at time step k. In other words, h creates the *model observation* from the prior state estimate. For the implementation of h, we converted from the Earth-fixed corotating International Terrestrial Reference Frame (ITRF) to the space-fixed Geocentric Celestial Reference Frame (GCRF $\approx$ J2000) using the sidereal-time rotation matrix (including the Equation of Equinoxes), precession, and nutation. In fact, all state vectors and orbital elements presented in this work are given in the J2000 frame. Note that an object state is fully characterized by a 6-dimensional state vector in Cartesian coordinates $\mathbf{x} = (x, y, z, \dot{x}, \dot{y}, \dot{z})$. However, each measurement only consists of a 2-dimensional tuple of observables $\mathbf{z} = (\alpha, \delta)$. Clearly, both f and h are highly nonlinear, which demontrates the need for a nonlinear filter like the UKF or the EKF.

As much as possible, we used the same initialisation parameters for the UKF and the EKF. In particular, we used the same initial state estimates, which we derived from operator-provided state estimates propagated to the time of the first observations. We further used a standard error of 2 arcsec in both right ascension and declination for all measurements. As an initial guess for the covariance matrix we used a diagonal matrix with variances for the position and velocity components of $(1000\,\mathrm{m})^2$ and $(1\,\mathrm{m\,s^{-1}})^2$, respectively. We also added process noise in equivalent matrix form with values of $(1\,\mathrm{m})^2$ for position and $(0.01\,\mathrm{m\,s^{-1}})^2$ for velocity.

In order to detect maneouvres, rather than directly analysing the residuals as defined in Eq. 2, we can define the *squared and normalized residuals* following [2] as

$$\varepsilon = \mathbf{y}^{\mathrm{T}}\,\mathbf{S}^{-1}\,\mathbf{y} \quad , \tag{3}$$

where $\mathbf{S}$ is the *innovation covariance matrix*, that is, the covariance matrix in measurement space. In addition, we can also utilize other quantities derived at every step in the UKF/EKF framework as maneouevre indicators, like the Mahalanobis distance and the Log-Likelihood (see Section 5).

For the calculation of the 13 sigma points that are necessary for a UKF working with 6-dimensional state vectors ($2 \times 6 + 1 = 13$), we follow the method of [19].

3.2. Conjunction analysis

In order to estimate the manoeuvre epochs and Δv-components, we follow the method presented by [6]. To be consistent and to simplify the analysis, we follow their approach of assuming all manoeuvres to be impulsive. Hence, for the remainder of this paper, the term manoeuvre epoch shall be used as meaning the epoch of the mid-point of the thruster-firing duration for a given manoeuvre.

For each manoeuvre that we identify, we start with two state estimates bracketing the manoeuvre. Note that these state estimates are not taken from the UKF/EKF directly, but rather come from a batch-least-squares OD process that takes all observations in the appropriate window between two consecutive manoeuvres into account. This way, the accuracy is slightly improved, as the UKF/EKF state estimates tend to "oscillate" around the true solution. We then sample the interval between the epochs of the two bracketing states in time steps of $10\,\mathrm{s}$ and numerically propagate the state vectors forward and backward in time, respectively.

The approximate manoeuvre epoch is then given by the epoch of minimum separation $d_{\min}$ between the forward- and backward-propagated (FWP, BWP) states [20]. Here, $d = |\mathbf{r}_{\mathrm{BWP}} - \mathbf{r}_{\mathrm{FWP}}|$ is the physical distance between the two states. We then calculate the encounter probability p for each step following the formalism given by [6, 1], which includes taking into account the covariance information. An improved estimate for the manoeuvre epoch can then be obtained by taking the epoch of maximum encounter probability $p_{\max}$ instead.

Finally, the manoeuvre Δv-components are obtained by simply taking the difference between the FWP and BWP states at the estimated manoeuvre epoch.

4. RESULTS

Three station-keeping manoeuvres were performed by both ASTRA-1KR and ASTRA-1L during the 9.5 days analysed in this work. The first two manoeuvres for each satellite were NS manoeuvres separated by one day, followed by an EW manoeuvre several days later. The effects of these manoeuvres on right ascension and declination is demonstrated in Figure 2, where we plot the differences in the numerically propagated models with and without taking manoeuvres into account. As can be seen, NS manoeuvres mainly affect the declination and have only a small effect on the right ascension, whereas EW manoeuvres strongly affect the right ascension but have no noticeable effect on the declination.

After initializing the filters as described in Sec. 3, we ran the predict-update-loops for the UKF and the EKF with the datasets for both satellites. The results are presented below.

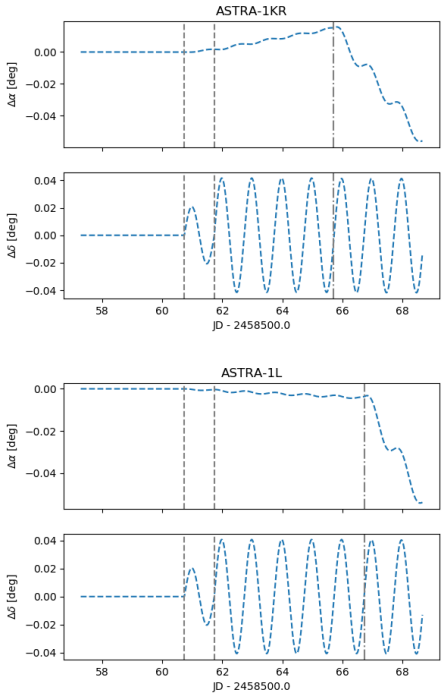

Figure 2. Effects of the station-keeping manoeuvres on right ascension and declination for ASTRA-1KR (upper panel) and ASTRA-1L (lower panel). The vertical grey lines indicate the manoeuvres (NS: dashed, EW: dash-dotted).

4.1. Unscented Kalman Filter

4.1.1. ASTRA-1KR

Figure 3 shows the evolution of right ascension and declination together with the UKF output, that is, the posterior state estimates $\mathbf{x}_k$ converted to measurement space. Manoeuvre epochs in this plot and all subsequent plots are indicated by grey vertical lines (NS: dashed, EW: dash-dotted). Note that the effect of the manoeuvres on the right ascension, as seen in Fig. 2, is not visible on this scale. Evidently, the filter closely follows the model curves. Consequently, the residuals in α and δ are centred around zero ($\bar{\alpha} = -0.03''$ (mean), $\tilde{\alpha} = 0.01''$ (median); $\bar{\delta} = -0.12''$, $\tilde{\delta} = -0.03''$), with an RMS of $1.33''$ in right ascension and $0.63''$ in declination, indicating a good filter performance (see Fig. 4). The small non-zero mean for δ is due to the short settling time that is required for the filter to converge again after each NS manoeuvre.

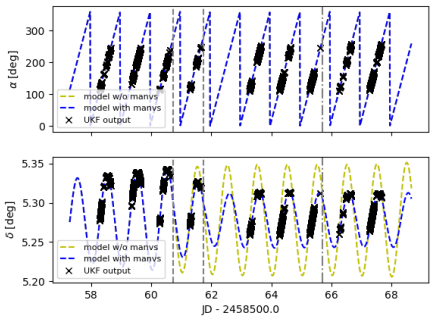

Figure 3. Evolution of right ascension (upper panel) and declination (lower panel) for ASTRA-1KR. The blue and yellow dashed curves represent the propagated model with and without taking manoeuvres into account, respectively. The black crosses show the UKF output and the vertical grey lines indicate the manoeuvres (NS: dashed, EW: dash-dotted).

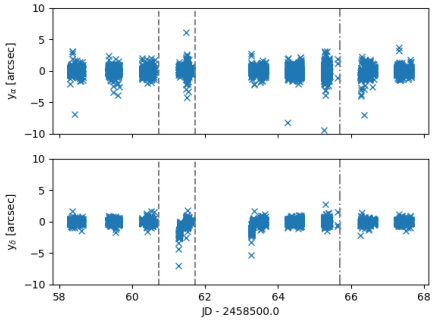

Figure 4. UKF residuals in right ascension (upper panel) and declination (lower panel) for ASTRA-1KR.

For illustration purposes, Fig. 5 shows the corresponding evolution of the semi-major axis and the inclination, as these quantities are good indicators for NS and EW station-keeping manoeuvres, respectively. After short settling phases at the very start of the filter loop and after each manoeuvre, the UKF converges quickly to the predicted states. This is particularly clear for the declination.

The squared and normalized residuals for the UKF, as defined in Eq. 3, are shown in Fig. 6. They exhibit brief but sharp increases after each NS manoeuvre, and are therefore a good indicator for these kinds of manoeuvres. The EW on the other hand is not detected by this indicator. For a discussion on the detectability of EW manoeuvres see Sec. 5.2.

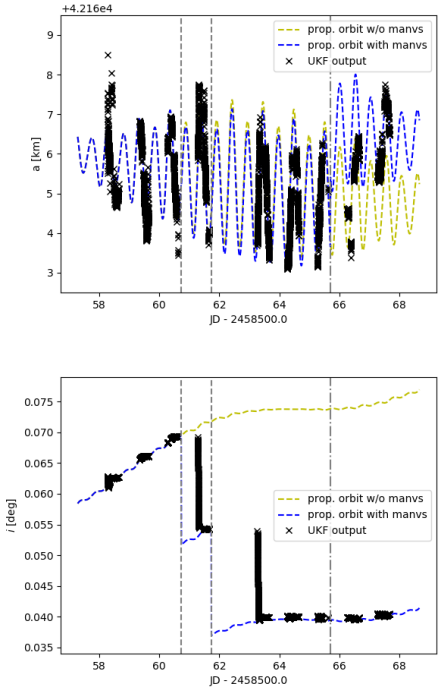

Figure 5. Evolution of the semi-major axis (upper panel) and the inclination (lower panel) for ASTRA-1KR.

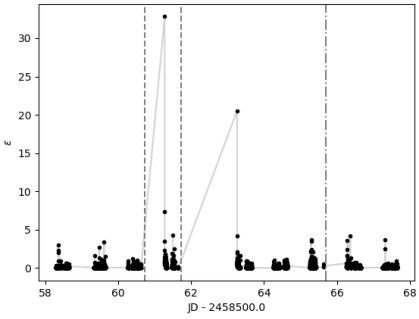

Figure 6. Squared and normalized UKF residuals for ASTRA-1KR.

4.1.2. ASTRA-1L

As in the previous section, Figure 7 shows the evolution of right ascension and declination together with the UKF output. Again, the filter closely follows the model curves. The corresponding residuals in α and δ are centred around zero ($\bar{\alpha} = -0.02''$, $\tilde{\alpha} = 0.00''$; $\bar{\delta} = -0.11''$, $\tilde{\delta} = -0.03''$), with an RMS of $1.42''$ in right ascension and $0.65''$ in declination (see Fig. 8).
Figure 9 shows the evolution of the semi-major axis and the inclination. As was the case for ASTRA-1KR, the UKF converges quickly to the predicted states after short settling phases at the very start of the filter loop and after each manoeuvre.
The squared and normalized residuals for the UKF are shown in Fig. 10. The NS manoeuvres are clearly detected, while the EW manoeuvre is not detected.

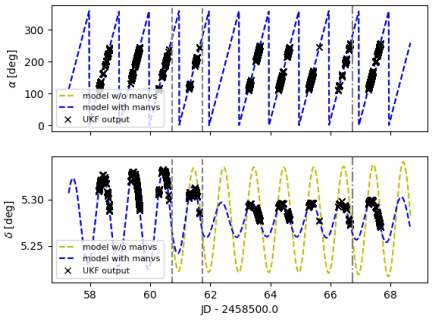

Figure 7. Evolution of right ascension (upper panel) and declination (lower panel) for ASTRA-1L. The blue and yellow dashed curves represent the propagated model with and without taking manoeuvres into account, respectively. The black crosses show the UKF output and the vertical grey lines indicate the manoeuvres (NS: dashed, EW: dash-dotted).

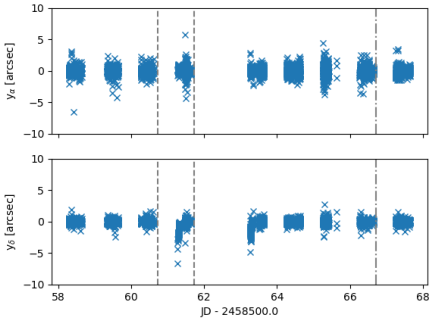

Figure 8. UKF residuals in right ascension (upper panel) and declination (lower panel) for ASTRA-1L.

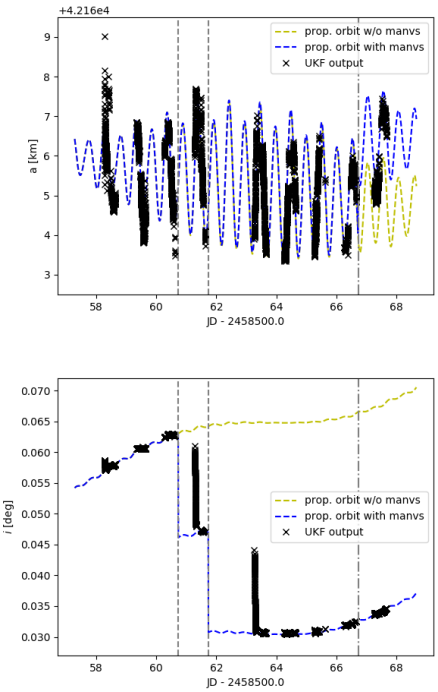

Figure 9. Evolution of the semi-major axis (upper panel) and the inclination (lower panel) for ASTRA-1L.

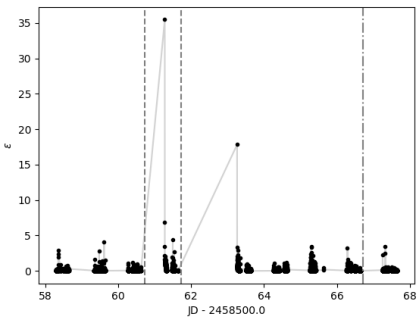

Figure 10. Squared and normalized UKF residuals for ASTRA-1L.

4.2. Extended Kalman Filter

4.2.1. ASTRA-1KR

In analogy to the previous sections, Figure 11 shows the evolution of right ascension and declination together with the EKF output. Again, the filter closely follows the model curves. The corresponding residuals in α and δ are centred around zero ($\bar{\alpha} = -0.02''$, $\tilde{\alpha} = 0.01''$; $\bar{\delta} = -0.12''$, $\tilde{\delta} = -0.03''$), with an RMS of $1.36''$ in right ascension and $0.63''$ in declination (see Fig. 12).
Figure 13 shows the evolution of the semi-major axis and the inclination. As was the case for UKF, the EKF also converges quickly to the predicted states after short

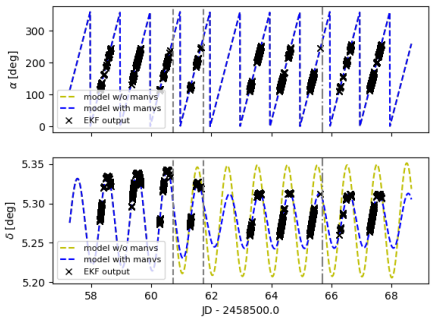

Figure 11. Evolution of right ascension (upper panel) and declination (lower panel) for ASTRA-1KR. The blue and yellow dashed curves represent the propagated model with and without taking manoeuvres into account, respectively. The black crosses show the EKF output and the vertical grey lines indicate the manoeuvres (NS: dashed, EW: dash-dotted).

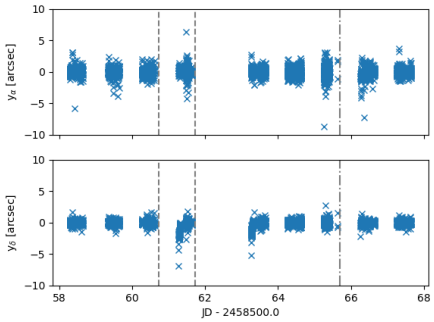

Figure 12. EKF residuals in right ascension (upper panel) and declination (lower panel) for ASTRA-1KR.

settling phases at the very start of the filter loop and after each manoeuvre.
The squared and normalized residuals for the EKF are shown in Fig. 14. The NS manoeuvres are clearly detected, while the EW manoeuvre is not detected.

4.2.2. ASTRA-1L

In analogy to the previous sections, Figure 15 shows the evolution of right ascension and declination together with the EKF output. Again, the filter closely follows the model curves. The corresponding residuals in α and δ are centred around zero ($\bar{\alpha} = -0.02''$, $\tilde{\alpha} = 0.00''$; $\bar{\delta} = -0.11''$, $\tilde{\delta} = -0.03''$), with an RMS of $1.40''$ in right ascension and $0.65''$ in declination (see Fig. 16).
Figure 17 shows the evolution of the semi-major axis and the inclination. Again, the EKF also converges quickly to the predicted states after short settling phases at the very start of the filter loop and after each manoeuvre.
The squared and normalized residuals for the EKF

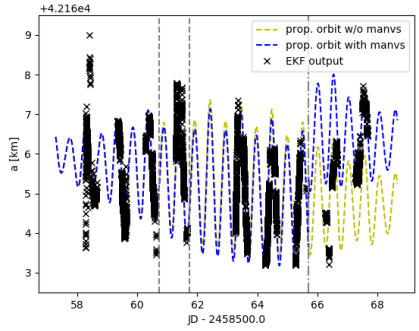

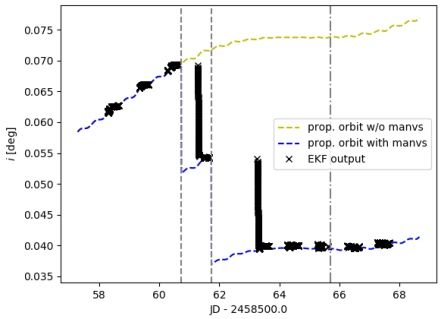

Figure 13. Evolution of the semi-major axis (upper panel) and the inclination (lower panel) for ASTRA-1KR.

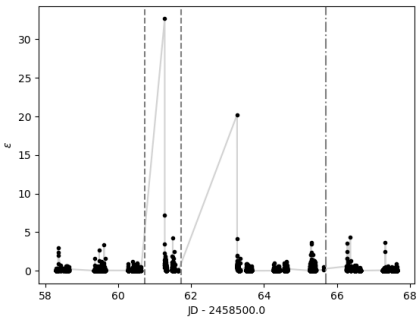

Figure 14. Squared and normalized EKF residuals for ASTRA-1KR.

are shown in Fig. 18. The NS manoeuvres are clearly detected, while the EW manoeuvre is not detected.

4.3. Manoeuvre Estimation

From the detection of a manoeuvre, we initially only know that it happened between two observation epochs. For the manoeuvres studied in this work, this window is always wider than 12 hours. As described in Sec. 3.2, we start with two state estimates at epochs that bracket the manoeuvre. Note that these epochs do not have to be the closest observations to the manoeuvre, and, in fact, we use a wider window than necessary for illustration pur-

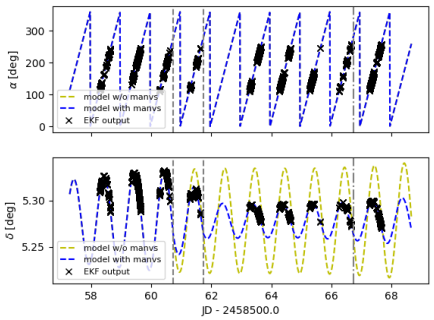

Figure 15. Evolution of right ascension (upper panel) and declination (lower panel) for ASTRA-1L. The blue and yellow dashed curves represent the propagated model with and without taking manoeuvres into account, respectively. The black crosses show the EKF output and the vertical grey lines indicate the manoeuvres (NS: dashed, EW: dash-dotted).

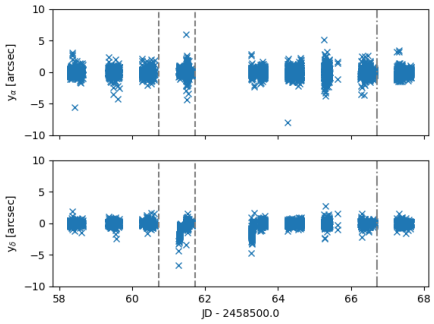

Figure 16. EKF residuals in right ascension (upper panel) and declination (lower panel) for ASTRA-1L.

poses. For this analysis we will focus on the NS manoeuvres that were successfully detected via the squared and normalized residuals.

We also tried our conjunction analysis method on the EW manoeuvres, but preliminary efforts did not result in good manoeuvre estimates. However, it should be noted that for the particular manoeuvres studied here, the magnitudes of the EW manoeuvres are less than 10% of the NS manoeuvre magnitudes, and thus they present a much more challenging scenario.

4.3.1. ASTRA-1KR

Figure 19 shows the encounter probability and the distance between the FWP and BWP states for the two NS manoeuvres of ASTRA-1KR. The true manoeuvre epochs and the epochs of the immediately adjacent observations are also shown for reference. Clearly, the locations of the maxima in the encounter probability correspond very well to the locations of the minima in the distance between the FWP and BWP states, although

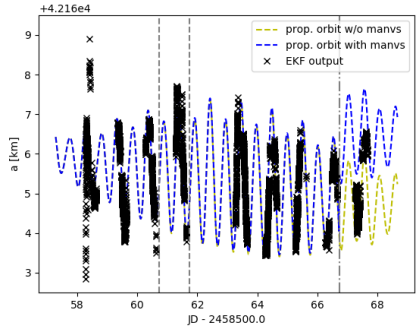

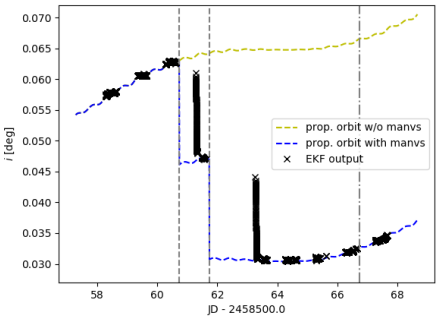

Figure 17. Evolution of the semi-major axis (upper panel) and the inclination (lower panel) for ASTRA-1L.

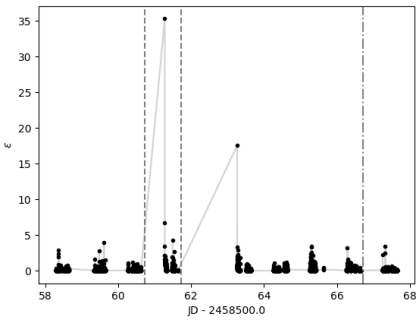

Figure 18. Squared and normalized EKF residuals for ASTRA-1L.

their respective epochs are not identical.

The deviations from the true manoeuvre epochs, $\Delta t = t_{\mathrm{calc}} - t_{\mathrm{true}}$, and Δv-components in the Radial-Tangential-Normal (RTN) frame, $\Delta(\Delta v_i) = \Delta v_{i,\mathrm{calc}} - \Delta v_{i,\mathrm{true}}$, for ASTRA-1KR obtained using both p_{max} and d_{min} are presented in Table 1. Using p_{max} results in significantly better estimates for the manoeuvre epochs as compared to using d_{min}.

4.3.2. ASTRA-1L

In analogy to the previous section, Fig. 20 shows the encounter probability and the distance between the FWP

Table 1. Deviations of manoeuvre epochs and Δv-components with formal uncertainties from operator data for the two NS manoeuvres of ASTRA-1KR.

		Δt [s]	$\Delta(\Delta v_r)$ [$\mathrm{m\,s^{-1}}$]	$\Delta(\Delta v_t)$ [$\mathrm{m\,s^{-1}}$]	$\Delta(\Delta v_n)$ [$\mathrm{m\,s^{-1}}$]
Man. #1	$p_{\max}$	-45	0.158 ± 0.170	-0.048 ± 0.068	-0.007 ± 0.002
	$d_{\min}$	-285	0.158 ± 0.173	-0.049 ± 0.062	-0.007 ± 0.002
Man. #2	$p_{\max}$	-4	0.093 ± 0.037	-0.059 ± 0.013	-0.007 ± 0.002
	$d_{\min}$	-174	0.093 ± 0.036	-0.059 ± 0.013	-0.007 ± 0.002

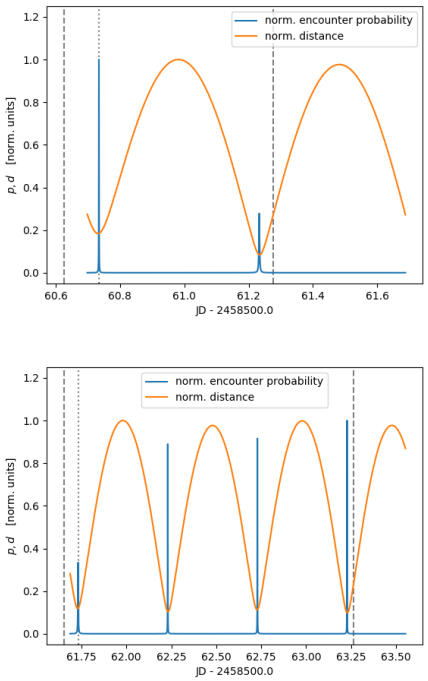

Figure 19. Encounter probability p and distance d between the FWP and BWP states ASTRA-1KR. The dotted grey vertical line indicates the true manoeuvre epoch, and the dashed grey vertical lines indicate the epochs of the adjacent observations.

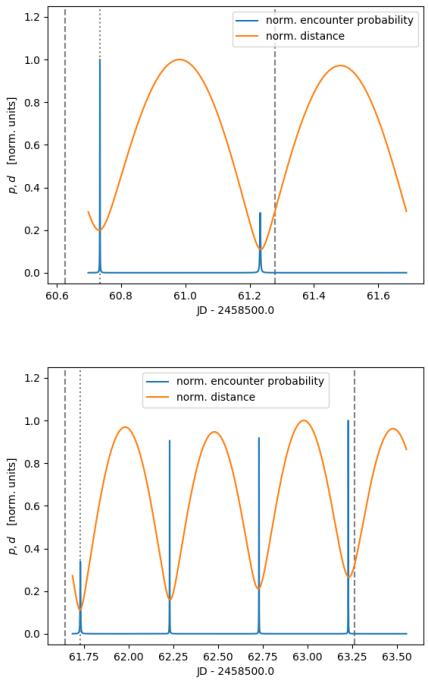

Figure 20. Encounter probability p and distance d between the FWP and BWP states ASTRA-1L. The dotted grey vertical line indicates the true manoeuvre epoch, and the dashed grey vertical lines indicate the epochs of the adjacent observations.

and BWP states for the two NS manoeuvres of ASTRA-1L. Again, the locations of $p_{\max}$ correspond very well to the locations $d_{\min}$ between the FWP and BWP states. Table 2 summarizes the conjunction analysis results for ASTRA-1L.

5. DISCUSSION

From the results presented in Sec. 4, it can be seen that the UKF and the EKF perform equally well. However, a truly fair comparison is virtually impossible, as both filters have different parameters that can be adjusted. For example, for the UKF we can adjust the parameters α, β, and κ, which determine how the sigma points are computed [19], but the same cannot be done for the EKF. In terms of computational speed, the EKF has a clear advantage, simply because for the UKF the state transition function must be called 13 times (once for each sigma point) for every step in the filter loop.

Following the detection of a manoeuvre, we have demonstrated the potential to determine the manoeuvre epoch to within less than a minute (or even a few seconds) using a conjunction analysis approach. The corresponding Δv-components in the radial and tangential directions can be determined to better than $20\,\mathrm{cm\,s^{-1}}$. For the normal

Table 2. Deviations of manoeuvre epochs and Δv-components from operator data for the two NS manoeuvres of ASTRA-1L.

		Δt [s]	$\Delta(\Delta v_r)$ [$\mathrm{m\,s^{-1}}$]	$\Delta(\Delta v_t)$ [$\mathrm{m\,s^{-1}}$]	$\Delta(\Delta v_n)$ [$\mathrm{m\,s^{-1}}$]
Man. #1	$p_{\max}$	-49	0.170 ± 0.184	-0.043 ± 0.074	-0.008 ± 0.002
	$d_{\min}$	-269	0.170 ± 0.187	-0.043 ± 0.068	-0.008 ± 0.002
Man. #2	$p_{\max}$	-21	0.095 ± 0.040	-0.052 ± 0.014	-0.028 ± 0.002
	$d_{\min}$	-201	0.094 ± 0.040	-0.052 ± 0.014	-0.028 ± 0.002

(out-of-plane) component, the results are even accurate to within 1-3 $\mathrm{cm\,s^{-1}}$, or, equivalently, to within 1-3% of the true values.

5.1. Alternative Indicators for NS-Manoeuvres

As already mentioned in Sec. 3.1, alternative but closely related indicators can be used for the detection of NS manoeuvres. For example, the Mahalanobis distance or the Log-Likelihood can be used [20].
The Mahalanobis distance D_M [13, 3]

$$D_M = \sqrt{\mathbf{y}^{\mathrm{T}}\,\mathbf{S}^{-1}\,\mathbf{y}} \quad , \tag{4}$$

is a statistical measure for the distance between a point and a distribution, and is equal to the square-root of the squared and normalized residuals ε as defined in Eq. 3.
The Log-Likelihood $\mathcal{L} = \log L$, that is, the natural logarithm of the filter likelihood function, is related to ε by the exponential function via

$$L = \frac{1}{\sqrt{2\pi\mathbf{S}}} \exp\left[-\frac{1}{2}(\mathbf{y}^{\mathrm{T}}\,\mathbf{S}^{-1}\,\mathbf{y})\right] \quad . \tag{5}$$

As an example, Figure 21 shows these quantities for the analysis of the ASTRA-1KR dataset with the UKF. Both NS manoeuvres are readily detected, albeit with slightly smaller significance compared to the squared and normalized residuals (Fig. 6).

5.2. Detection of EW Manoeuvres

The indicators discussed so far are very sensitive to NS manoeuvres, yet they do not produce reliable detections of EW manouvres. In the case of GEO orbits, we can make the assumption that EW manoeuvres can only have non-zero Δv-components in the x- and y-directions, that is, that the out-of-plane component is zero[1]. In analogy to

[1]For other orbit configurations the preceding analysis has to be performed in the RTN frame.

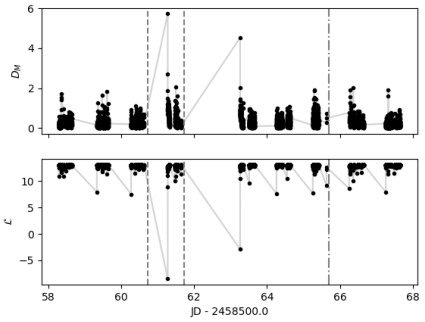

Figure 21. Mahalanobis distance (upper panel) and Log-Likelihood (lower panel) from the UKF analysis of ASTRA-1KR data.

Eq. 3, we can define the squared and normalized residuals in state space as

$$\xi^* = (\mathbf{x} - \bar{\mathbf{x}})^{\mathrm{T}}\,\bar{\mathbf{P}}^{-1}\,(\mathbf{x} - \bar{\mathbf{x}}) \quad . \tag{6}$$

Here, $\bar{\mathbf{P}}$ is the prior covariance matrix. Note that we are now using the difference between the posterior state $\mathbf{x}$ and the prior state $\bar{\mathbf{x}}$ instead of the filter residuals, and that we have dropped the indices k for clarity. However, the uncertainties in the prior (predicted) state estimate can be quite large if there are longer gaps in the observation time series, potentially hiding manoeuvres. If we instead look at the equivalent un-normalized quantities $\xi_i = (\mathbf{x}_i - \bar{\mathbf{x}}_i)^2$ for individual components, and single out position- and velocity-components in the x-y-plane, we can define the auxiliary quantity

$$\xi_{xy} = \sqrt{\xi_x^2 + \xi_y^2 + \xi_{v_x}^2 + \xi_{v_y}^2} \quad , \tag{7}$$

which we call the *squared in-plane residuals*, and which can be used for a tentative detection of the EW manoeuvres. Adopting a heuristic approach, we can further enhance the significance of the peak by normalizing with the posterior variances, i.e. we define the *squared and normalized in-plane residuals* as

$$\xi_{xy}^0 = \sqrt{\frac{\xi_x^2}{\sigma_x^2} + \frac{\xi_y^2}{\sigma_y^2} + \frac{\xi_{v_x}^2}{\sigma_{v_x}^2} + \frac{\xi_{v_y}^2}{\sigma_{v_y}^2}} \quad . \tag{8}$$

Table 3. Deviations of manoeuvre epochs from operator data and absolute Δv-components in the RTN frame for the four possible solutions found using $p_{\max}$ for the second NS manoeuvre of ASTRA-1KR. Here, the first peak is the true peak.

	Δt [s]	$\Delta(\Delta v_r)$ [$\mathrm{m\,s^{-1}}$]	$\Delta(\Delta v_t)$ [$\mathrm{m\,s^{-1}}$]	$\Delta(\Delta v_n)$ [$\mathrm{m\,s^{-1}}$]
operator data	–	**0.003**	**-0.004**	**0.983**
peak #1	-4	0.096 ± 0.037	-0.064 ± 0.013	0.976 ± 0.002
peak #2 [+12 h]	-124	0.085 ± 0.181	0.064 ± 0.048	-0.975 ± 0.002
peak #3 [+24 h]	-244	0.090 ± 0.246	-0.064 ± 0.067	0.976 ± 0.002
peak #4 [+36 h]	-374	0.079 ± 0.389	0.064 ± 0.115	-0.975 ± 0.002

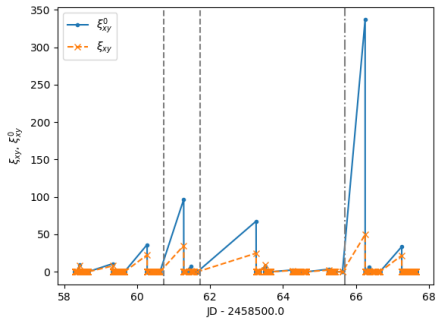

Figure 22. Squared and normalized in-plane residuals (blue) and squared in-plane residuals from the UKF analysis of ASTRA-1KR data.

As an example, Fig. 22 shows these residuals for the UKF analysis of ASTRA-1KR. As can be seen, the EW manoeuvre causes a sharp rise in ξ^0_{xy}, which is less pronounced in ξ_{xy}. The NS manoeuvres only result in modest peaks. Note that ξ^0_{xy} is susceptible to any large deviations of the measurements from the prior (predicted) state estimate even if they are not due to a manoeuvre. However, the same is true for ε, as in both cases we *want* the filter to trip over these measurements.

5.3. Ambiguity of NS Manoeuvre Epochs

During the conjunction analysis presented in Sec. 4.3, we encountered ambiguities in the determination of the manoeuvre epochs and corresponding Δv-components. Due to the nature of geocentric orbits, the separation between the FWP and BWP states takes on a minimum approximately every 12 hours. The same is true, of course, for the maxima of the collision probability. This 12-hr periodicity is due to the fact that NS station-keeping manoeuvres are generally performed at times of node crossings, that is, whenever the orbital plane intersects the celestial equator. That way, any out-of-plane impulse only affects the inclination.
As can be seen from Figures 19 and 20 and the results in Tables 1 and 2, if the node-crossing window is known, then this technique can produce estimates for the manoeuvre epochs accurate to within less than a minute, or even to within a few seconds in some cases. However, if the manoeuvre time cannot be constrained to within two consecutive node crossings, an ambiguity arises in the estimation of the manoeuvre epoch, as there are several maxima in $p_{\max}$ (or several minima in $d_{\min}$).
Fortunately, for GEO satellites, the manoeuvre epoch can at least be determined modulo an integer multiple of 12 hours. The corresponding Δv-components also do not change much, except for a sign flip every 12 hours. Effectively, this means that even if there are data gaps spanning several node crossings and thus the estimated manoeuvre epoch may be off by an integer multiple of 12 hours, the result of any subsequent orbital solution is almost as good no matter which peak of $p_{\max}$ is selected. As an example, Table 3 summarizes the manoeuvre estimates we obtained using $p_{\max}$ for the four peaks in the lower panel of Fig. 19, which demonstrates the ambiguity for the second NS manoeuvre of ASTRA-1KR. Note that the increase in the formal uncertainties is caused by the longer propagation times.

6. OUTLOOK

For this study, we implemented prototypes of an EKF and a UKF that can detect manoeuvres in passive-optical observations taken with the SMARTnet telescope network. An improved, fully automated version will eventually be applied to all observations taken with the SMARTnet telescope network.
We have assumed that the object correlation for our observations had been successful in the first place. While beyond the scope of this work, this problem is closely related to and a necessary prerequisite for manoeuvre detection, and is a highly topical field of research (e.g. [15]). A working object-correlation algorithm needs to be incorporated in any automated data processing system or database.
As mentioned in Section 3, we also made the assumption of impulsive manoeuvres. A more sophisticated orbit estimation could include and integrate over a non-zero manoeuvre duration, as the Δv-components are given in

the RTN frame, the orientation of which changes with respect to a geocentric frame over the thruster-firing duration (e.g. [10]).
Clearly, if a manoeuvre is detected and its epoch and Δv-components are estimated, any subsequently run OD algorithm (e.g. a batch-least-squares filter), will be able to produce a much more accurate orbit estimate compared to an estimate derived without knowledge of the manoeuvre. On top of that, the manoeuvre epoch and the Δv-components can be included as free parameters in the OD. Potentially, as suggested in [20], by using the manoeuvre estimates from the conjunction analysis as input values, the manoeuvre epoch and Δv-components may be further refined.

ACKNOWLEDGMENTS

The authors would like to thank SES S.A. for providing orbit and manoeuvre information for the ASTRA-1KR and ASTRA-1L satellites studied in this work. We would further like to thank Carolin Früh for many inspiring and fruitful discussions.

REFERENCES

1. Alfano, S, (2005). Relating Position Uncertainty to Maximum Conjunction Probability. *The Journal of the Astronautical Sciences*, **53**(2), 193-205

2. Bar-Shalom Y., Xiao-Rong L., Kirubarajan T., (2001). *Estimation with applications to tracking and navigation*, Wiley

3. De Maesschalck R., Jouan-Rimbaud D., Massart D. L.,(2000). The Mahalanobis distance, *Chemometrics and Intelligent Laboratory Systems*, **50**(1), 1–18

4. Fiedler H., Herzog J., Ploner M., et al., (2017). SMARTnet™– First Results of the Telescope Network, in: Proc. of the 7th European Conference on Space Debris, Darmstadt, Germany

5. Flohrer T., Schildknecht T., Früh C., Musci, R., Ploner, M., (2007). Optical Observations at the Zimmerwald Observatory, in: Proc. of the 58th International Astronautical Congress, Hyderabad, India

6. Herzog J., Fiedler H., Schildknecht T., (2017). Using Conjunction Analysis Methods for Manoeuvre Detection, in: Proc. of the 7th European Conference on Space Debris, Darmstadt, Germany

7. Jiang Y., Yang H., Baoyin H., Ma P., (2019). Extended Kalman Filter with Input Detection and Estimation for Tracking Manoeuvring Satellites, *The Journal of Navigation*, **72**(3), 628-648

8. Julier S. J., Uhlmann J. K., (1997). New extension of the Kalman filter to nonlinear systems, in: Proc. SPIE 3068, Signal Processing, Sensor Fusion, and Target Recognition VI

9. Kalman, R. E., (1960). A New Approach to Linear Filtering and Prediction Problems. *Journal of Basic Engineering*, **82**, 35-45

10. Kelecy T., Jah M., (2010). Detection and orbit determination of a satellite executing low thrust maneuvers, *Acta Astronautica*, **66**, 798-809

11. Kelecy T., Hall D., Hamada K., Stocker M. D., (2007). Satellite Maneuver Detection Using Two-Line Element (TLE) Data, in: Proceedings of the Advanced Maui Optical and Space Surveilllance (AMOS) Technologies Conference, Maui, Hawaii, USA

12. Lemmens S., Krag H., (2014). Two-Line-Elements-Based Maneuver Detection Methods for Satellites in Low Earth Orbit, *Journal of Guidance, Control, and Dynamics*, **37**(3), 860-868

13. Mahalanobis P. C., (1936). On the generalised distance in statistics, *Proceedings of the National Institute of Sciences of India*, **2**(1), 49–55

14. Rauch H. E., Tung F., Striebel C. T., (1965). Maximum Likelihood Estimates of Linear Dynamic Systems, *AIAA Journal*, **3**(8), 1445-1450

15. Serra R., Yanez C., Früh C., (2021). Tracklet-to-orbit association for maneuvering space objects using optimal control theory, *Acta Astronautica*, **181**, 271-281

16. Shrivastava S. K., (1978). Orbital Perturbations and Stationkeeping of Communication Satellites, *Journal of Spacecraft and Rockets*, **15**(2), 67-78

17. Song W. D., Wang R. L., Wang J., (2012). A simple and valid analysis method for orbit anomaly detection, *Advances in Space Research*, **49**, 386-391

18. Teixeira B. O. S., Santillo M. A., Erwin R. S., Bernstein D. S., (2008). Spacecraft Tracking Using Sampled-Data Kalman Filters, *IEEE Control Systems Magazine*, **28**(4), 78-94

19. Van der Merwe R., (2004). Sigma-point kalman filters for probabilistic inference in dynamic state-space models, Dissertation, Oregon Health & Science University

20. Zollo A., (2020). Satellite maneuver detection and estimation using optical measurements, MSc thesis, Institut Supérieur de l'Aéronautique et de l'Espace and Deutsches Zentrum für Luft- und Raumfahrt